ACS APPLIED ENERGY MATERIALS

www.acsaem.org
Article

Fast Joule Heating Preparation and Performance Study of Carbon-Loaded Nano Tungsten-Based Electrocatalysts for Highly Efficient Oxygen Evolution Reaction

Pengchong Shen, Lili Guan,* Zhekai Zhang, Jiaming Zhao, Yaqi Yang, Li Wu, Yarong Huang, Menggang Li, and Xiwen Song

Cite This: https://doi.org/10.1021/acsaem.5c00500

Read Online

ACCESS | Metrics & More | Article Recommendations | Supporting Information

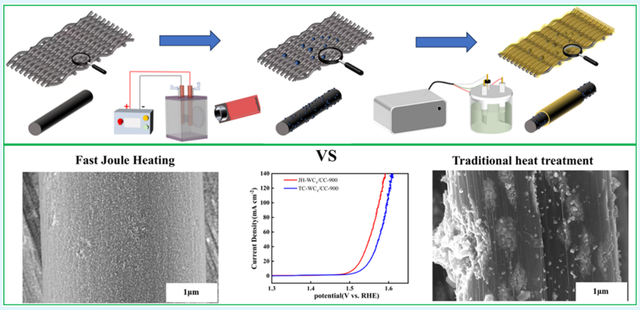

ABSTRACT: Water electrolysis has attracted the attention of many researchers as a green energy production pathway. However, the oxygen evolution reaction challenges the advancement of green energy from electrolytic water due to slow reaction kinetics and high overpotential. In this study, highly dispersed WC_x nanoparticles on carbon cloth (CC) with good self-supporting properties were rapidly synthesized using flash Joule heating for 180 s. At the same time, the nonequilibrium ultrarapid impact process due to Joule heating makes it possible to have more defects in the integrated electrodes. As a result, JH-WC_x/CC-900, which has been heat-treated at 900 °C, shows an excellent performance in alkaline media. To further enhance its electrocatalytic performance, the NiFe-LDH cladding layer was prepared on JH-WC_x/CC-900 by a one-step electrodeposition technique, taking advantage of the synergistic effect between different components. The Ni_5Fe_5-LDH/WC_x/CC electrode material showcased superior electrocatalytic performance in an alkaline medium, with a low overpotential of 215 mV at 10 mA cm^{-2} and a Tafel slope of 45.71 mV dec^{-1}. The proposed synthesis and design strategy opens up a fast and simple route for the rapid synthesis of carbide catalysts.

KEYWORDS: *oxygen evolution reaction, flash Joule heating, electrodeposition, nanoparticles, WC_x*

1. INTRODUCTION

With the rise of the global economy, the depletion of fossil energy sources, and the deterioration of the global environment, it has become imperative to explore a sustainable, green, and clean alternative to fossil energy sources. Hydrogen is the most promising green and clean energy source for the future. Hydrogen can be obtained through Electrochemical Water Splitting (EWS), and the Oxygen Evolution Reaction (OER) is the key anode reaction in the EWS. The overall electrochemical water-splitting reaction is kinetically slow. It has a high overpotential due to the 4-electron transfer involved in the OER, which requires higher energy than the cathodic Hydrogen Elimination Reaction (HER).[1−5] The OER process controls the overall efficiency of the electrochemical water cracking reaction; therefore, studying a superior OER electrocatalyst can effectively improve the overall efficiency of water cracking.

Currently, RuO_2 and IrO_2 are the most efficient and stable catalysts in OER, but characteristics such as scarcity and high cost have prevented large-scale production applications.[6,7] Researchers have recently used single-atom catalysts, transition metal oxides, sulfides, carbides, and their hydroxides as efficient OER catalysts.[8] Metal Carbides, such as WC_x, MoC_x, and so on, have attracted the attention of many researchers due to their advantages of low cost, low overpotential, and high electronic conductivity.

Diao et al.[9] used a hydrothermal method to prepare WN/WC heterostructures on nickel foam NF, which significantly accelerated the charge transfer and thus improved the electrocatalytic efficiency, and the catalyst exhibited a low overpotential of 320 mV at 10 mA cm^{-2} in the oxygen evolution reaction in 1 M KOH solution. In a novel development, a catalyst comprising Ni/Mo_xC (MoC, Mo_2C) nanoparticle-loaded n-doped graphene/carbon nanotube hybrid (NC) has been engineered by Das et al.[10] This achievement represents a significant advancement in the field, achieved through a straightforward one-step hydrothermal integration strategy. The core finding of the study is the demonstration of an electronic synergistic effect between

Received: February 18, 2025
Revised: May 6, 2025
Accepted: May 14, 2025

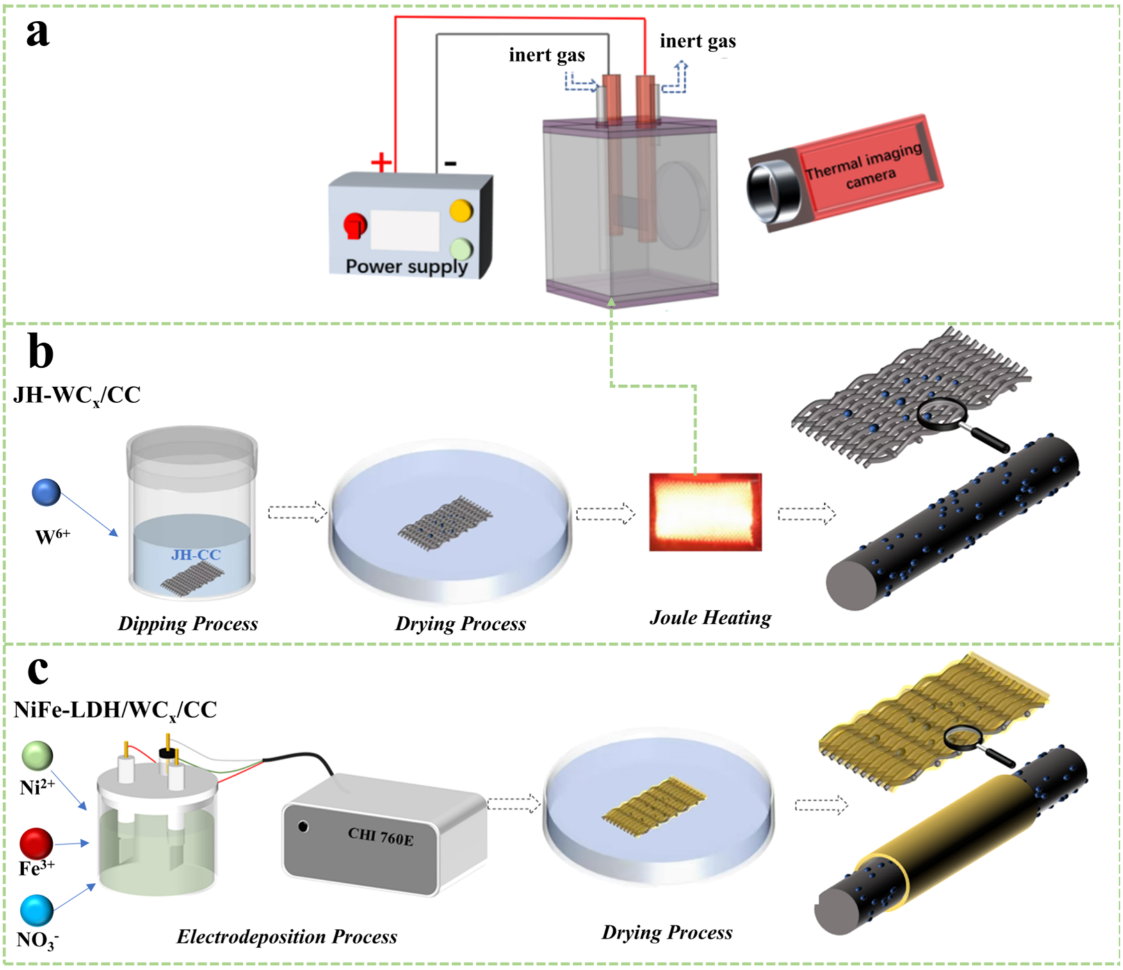

Figure 1. (a) Device diagram used for Joule heating, (b) synthesis process of the JH-WC$_x$/CC catalyst, (c) synthesis process of the NiFe-LDH/WC$_x$/CC catalyst.

Mo$_x$C, Ni, and NC. The catalyst was characterized by a low overpotential of 328 mV at 10 mA cm^{-2} in a 1 M KOH solution. Wang et al.[11] proposed ultrasmall core–shell FeNi encapsulated in tungsten carbide, stabilized in a thin N-doped graphitized carbon layer (NCL), and their prepared FeNi@WC-NCL catalyst exhibited a low overpotential of 279 mV at 10 mA cm^{-2} in 1 M KOH solution. The above-mentioned tungsten carbide catalysts have now become one of the important OER catalysts researched at home and abroad due to their natural abundance, environmental friendliness, and high catalytic activity.

However, the preparation of WC usually requires a long period of high-temperature treatment, which inevitably causes agglomeration of tungsten carbide (WC) particles, resulting in a lack of active sites and thus affecting its catalytic performance.[12] In recent years, Joule heating has been proven to be very advantageous in synthesizing highly dispersed nanomaterials. The Joule heating technique has now successfully enabled the preparation of a wide range of nanomaterials, including monometallic nanoparticles (e.g., Al, Sn, Pd, Ag, and Ir),[13−16] compound nanoparticles (SiC, FeS$_2$, CoS, Co$_3$O$_4$, and MoS$_2$),[17−20] and high-entropy nanoparticles (CoMoFeNiCu, PtPdRhRuCe, and PtPdCoNiFeCuAuSn)[21,22] among others. In this paper, highly dispersed WC$_x$ nanocatalysts were rapidly synthesized using carbon cloth as a material substrate via an impregnation-fast Joule heating technique. On the one hand, the high electrical conductivity and good heat radiation of the carbon cloth, when an electric current is passed, the carbon cloth rapidly rises to the temperature required for catalyst synthesis. At the same time, the carbon cloth can be used as a carbon source for carbothermal reduction. It is interesting that this temperature is lower than the phase formation temperature required by traditional heat treatment, and which avoided the problem of particles agglomeration in the traditional heat treatment process. At the same time, the ultrafast temperature change of Joule heating makes the material produce more defect structures, thus enhancing its electrocatalytic activity.

However, the inherent adsorption and dissociation capacities of single-component catalysts limit their reactivity.[23,24] Moreover, the surface active sites of NiFe layered double hydroxides (LDHs) have a strong adsorption capacity for hydroxyl groups. In this work, in order to further improve the OER performance, NiFe-LDH was successfully coated via the electrodeposition method on the surface of highly dispersed nano-WC$_x$ to form a self-supporting integrated electrode Ni$_y$Fe$_{10-y}$-LDH/WC$_x$/CC. The catalytic performance was further improved by the synergistic effect between different components. The results show that Ni$_5$Fe$_5$-LDH/WC$_x$/CC exhibits excellent activity in alkaline electrolytes with a low overpotential of 215 mV at 10 mA cm^{-2}.

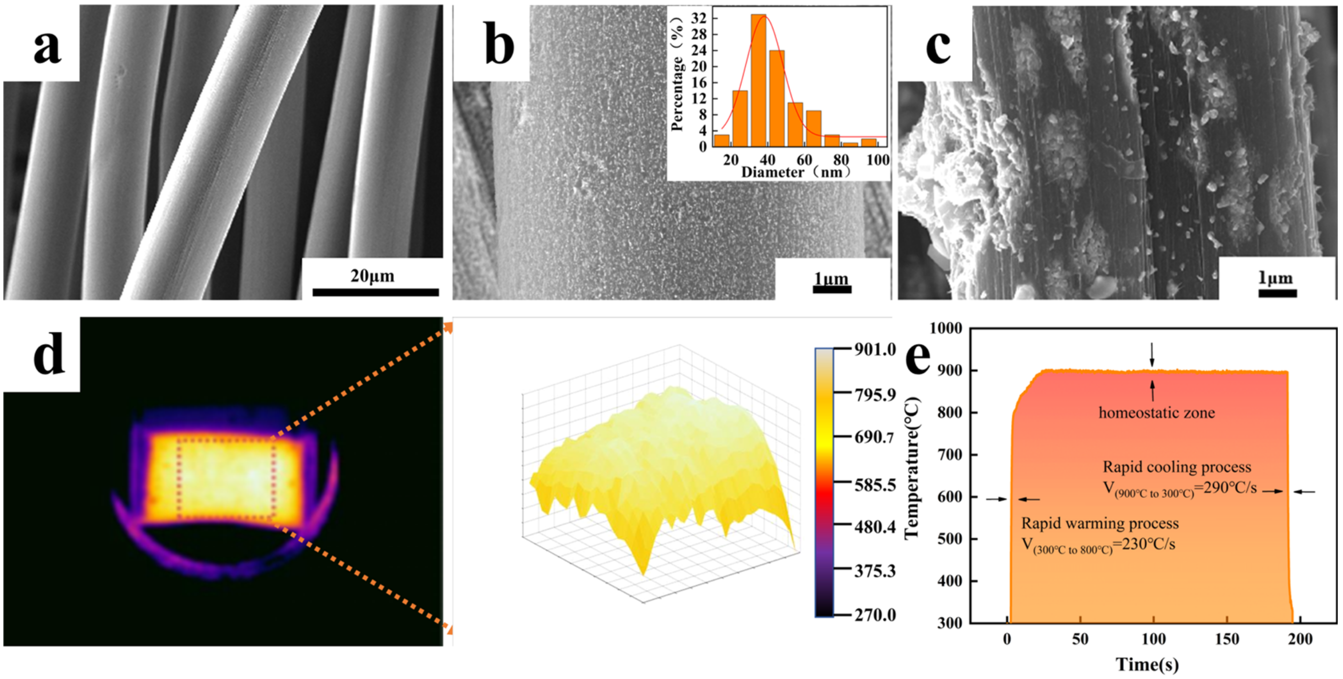

Figure 2. (a−c) SEM images of JH-CC, JH-WC_x/CC-900, TC-WC_x/CC-900, (d) surface temperature distribution and 3-D Gradient of Carbon Cloth. (e) Curve of temperature rise and fall as a function of time for Joule heating.

In this work, highly uniformly distributed carbon-loaded nanoparticles of tungsten carbide were prepared ultrafast by using Joule heating, which effectively suppressed the sintering agglomeration problem of carbide during the conventional heat treatment process and provided a new way of constructing loaded carbide materials. For the first time, NiFe-LDH was successfully coated on the surface of WC_x to form a self-supporting NiFe-LDH/WC_x integrated electrode, and the catalytic performance was further improved by the synergistic effect between different components.

2. EXPERIMENTAL SECTION

2.1. Materials and Reagents. All of the reagents were used as purchased without further purification. Tungsten chloride (WCl_6, 99%), iron nitrate nonahydrate ($Fe(NO_3)_3 \cdot 9H_2O$, 99.99%), nickel nitrate hexahydrate ($Ni(NO_3)_2 \cdot 6H_2O$, AR), and ethanol absolute were purchased from Aladdin. Carbon cloth (CC, WOS1009) was obtained from Carbon Energy. All experiments use ultrapure water.

2.2. Preparation of Carriers and Catalysts. *2.2.1. Preprocessing of CC.* Joule heat activation of carbon cloth CC was carried out using our previous work,[25] as shown in Figure 1a, and the activated CC carrier is abbreviated as JH-CC. The specific process is by applying direct current to the empty carbon cloth (1 cm × 3 cm) with the aid of copper electrode clamps in a nitrogen atmosphere. The activated carbon cloth is produced following heat treatment at a temperature of 800 °C for 60 s, a process facilitated by the rapid heating generated by Joule heating. The temperature was measured by an infrared thermal imager.

2.2.2. Preparation of WC_x/CC. One mmol of tungsten hexachloride was poured into 20 mL of anhydrous ethanol solution for a sealed reaction for 6 h. The JH-CC substrate, which was activated as described above, was impregnated in this solution for 12 h at room temperature. Subsequently, the dry precursor supported by a carbon cloth was subjected to Joule heating. When using Joule heating, the peak temperature (800, 900, 1000, and 1100 °C) of Joule heating can be controlled by adjusting the current at a constant voltage (25 V). And the sample was recorded as JH-WC_x/CC-*T*, *T* is the temperature. The process is shown in Figure 1b.

To make a comparison with conventional sintering, carbon cloth loaded with precursors was calcined in a tube furnace in an argon atmosphere at 900 °C for 2 h. The sample was noted as TC-WC_x/CC-900.

2.2.3. Synthesis of NiFe-LDH/WC_x/CC. NiFe-LDH was prepared on the surface of WC_x/CC by using an electrodeposition technique. The electrodeposition was carried out in a three-electrode system, applying Ag/AgCl as the reference electrode, a graphite rod as the auxiliary electrode, and a piece of JH-WC_x/CC (1 cm × 2 cm) as the working electrode, respectively. A 50 mL deposition solution of 0.06 M consisted of $Ni(NO_3)_2 \cdot 6H_2O$ and $Fe(NO_3)_3 \cdot 9H_2O$ in different ratios (10/0, 7/3, 5/5, 3/7, 0/10) and electrodeposited at a constant potential of −1 V for 10 min. After deposition, the electrodes were cleaned with deionized water and dried in an oven at 60 °C. The samples prepared were labeled Ni_yFe_{10-y}-LDH/WC_x/CC. The preparation process is shown in Figure 1c.

2.3. Physicochemical Characterizations. X-ray diffraction (XRD, Bruker D8) analysis was used to investigate the crystallinity of samples with a scanning rate of 5°/ min in the range between 20 and 80° (2θ) using an X-ray source of Cu Kα and operating parameters of 0.1541 nm (wavelength), 30 kV (voltage), and 10 mA (current). The microscopic morphology of the samples was observed by scanning electron microscopy (SEM, TESCAN CLARA) with energy dispersive spectrometry (EDS) mapping to further observe the morphology of the samples and the exposed surfaces. The samples used in this experiment were not sprayed with gold. The surface electronic states of the samples were characterized by using X-ray photoelectron spectroscopy (XPS, Thermo Scientific ESCALAB 250Xi) with C 1s (284.8 eV) as a calibration reference and processed by fitting analysis using Avantage software. The various parameters of the XPS are Al Kα (hv = 1486.6 eV), power 150 W, 650 μm beam spot, voltage 14.8 kV, current 1.6 A.

The thermal infrared imager (FOTRIC-626CH, Shanghai Thermal Imaging Technology Co, Ltd.) was used to monitor the actual temperature distribution of the samples and the changes in the rate of temperature rise and fall. The TG analyzer (NETZSCH STA 449 F3) was used to test the mass change of the precursor during heating at a temperature range from room temperature to 1200 °C with a heating rate of 10 °C min^{-1} in N_2 atmosphere. The morphology and percent composition of the samples were observed by using a transmission

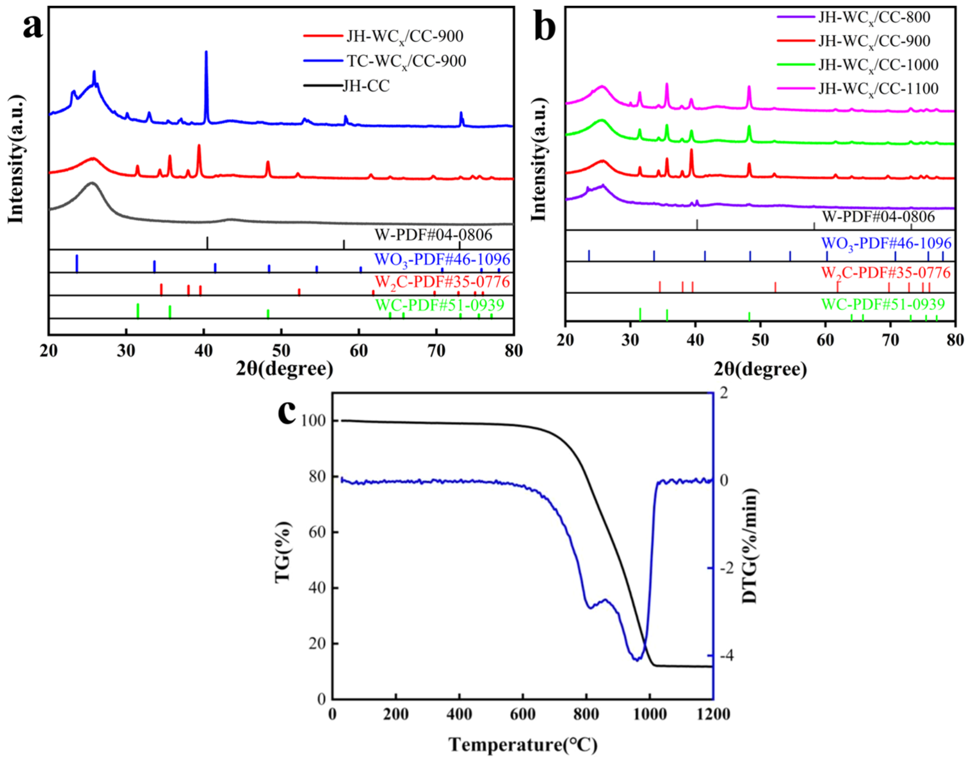

Figure 3. (a) X-ray diffraction patterns of empty carbon cloth and catalysts obtained by different heat treatments, (b) the effect of Joule heat treatment temperature on phase structure, and (c) TG-DTG curves of precursors.

electron microscope (Tecnai G2 F30 S-TWIN) instrument equipped with an energy probe. Atomic force Raman spectroscopy (LabRAM Odyssey Nano HORIBA Japan) is used to test the degree of graphitization of samples in the wavelength range 1000−1800 cm^{-1}. ICP-MS is an inductively coupled plasma mass spectrometer (PerkinElmer NexION 300D ICP-MS, PerkinElmer) used to detect the presence of metal ions in the solution before and after the stability test.

All relevant electrochemical tests were carried out at room temperature in a three-electrode, single-compartment cell with 1.0 M KOH electrolyte using a CHI 760E electrochemical workstation. Hg/HgO was used as a reference electrode, graphite rods (Φ 6 mm) were used as auxiliary electrodes, and the prepared carbon cloth integrated electrode was directly used as the working electrode (1 cm^2). The volume of electrolyte is 50 mL and the distance between the three electrodes is 2 cm. Samples were CV activated for 20 turns prior to electrochemical testing and ranged from 0.9268 to 1.9268 V (vs RHE). Polarization curves were obtained by linear scanning voltammetry (LSV) over the 0.9268−1.9268 V (vs RHE) potential range and at a scan rate of 5 mV s^{-1}(Manual *iR* compensation = 90%). Stability tests were performed at a current density of 10 mA cm^{-2} by using time amperometry. Electrochemical impedance spectroscopy (EIS) was performed in the range of 1 Hz to 100 kHz with the applied potential of 1.6268 V (vs RHE). The electrochemical double layer capacitance (C_{dl}) was determined from the scan rates (20, 40, 60, 80, 100 mV s^{-1}) at different scan rates in the potential range used where CV curves were determined. All potential reported in this work were converted to the corresponding potentials relative to the reversible hydrogen electrode (RHE) using the following equation:

$$E_{RHE} = E_{Hg/HgO} + 0.098\ V + 0.0592 \times pH$$

3. RESULTS AND DISCUSSION

3.1. OER Study of WC$_x$/CC.

As illustrated in Figure 2a,b, the microscopic morphologies of Joule heat-treated empty carbon cloths (JH-CC) and JH-WC$_x$/CC-900, respectively, is evident. Figure 2c demonstrates the morphology of a comparison sample (TC-WC$_x$/CC-900) subjected to conventional heat treatment in a nitrogen atmosphere within a tube furnace. It is evident that the carbon cloth sample, designated as JH-CC, exhibits a pristine and smooth surface that is devoid of any impurities. The micromorphology of JH-WC$_x$/CC-900, obtained by thermal shock, is demonstrated in Figure 2b, where there is clear evidence of highly dispersed nanoparticles on the surface of the carbon fiber with a uniform distribution. The inset displays a narrow particle size distribution, with an average grain size of 44 nm and a total loading of 2.13 mg/cm^2. In contrast, comparing the conventional heat-treated sample TC-WC$_x$/CC-900 (Figure 2c), the catalysts prepared by the same heat treatment temperature have a very serious agglomeration phenomenon on the surface of the carbon fiber, which is not uniformly distributed. The EDS spectra of JH-WC$_x$/CC-900 and TC-WC$_x$/CC-900 (Figure S1) also show that the surface of JH-WC$_x$/CC-900 is uniformly distributed, while the surface of TC-WC$_x$/CC-900 is heavily agglomerated.

Figure 2d,e shows the surface temperature distribution and temperature variation of the carbon cloth loaded with tungsten precursor during the Joule heating process. The results show that the temperature field of the samples monitored by the infrared camera is uniformly distributed, and the samples were warmed up from 300 to 900 °C in 2.18 s, with the fastest warming rate of 260 °C/s, and the temperature decreased from 900 to 300 °C in 2.06 s during the cooling process, with a cooling rate of 290 °C/s. This ultrafast, nonequilibrium high-temperature thermal shock technique enables the synthesis of uniformly dispersed nanoparticles on carbon carriers in a short

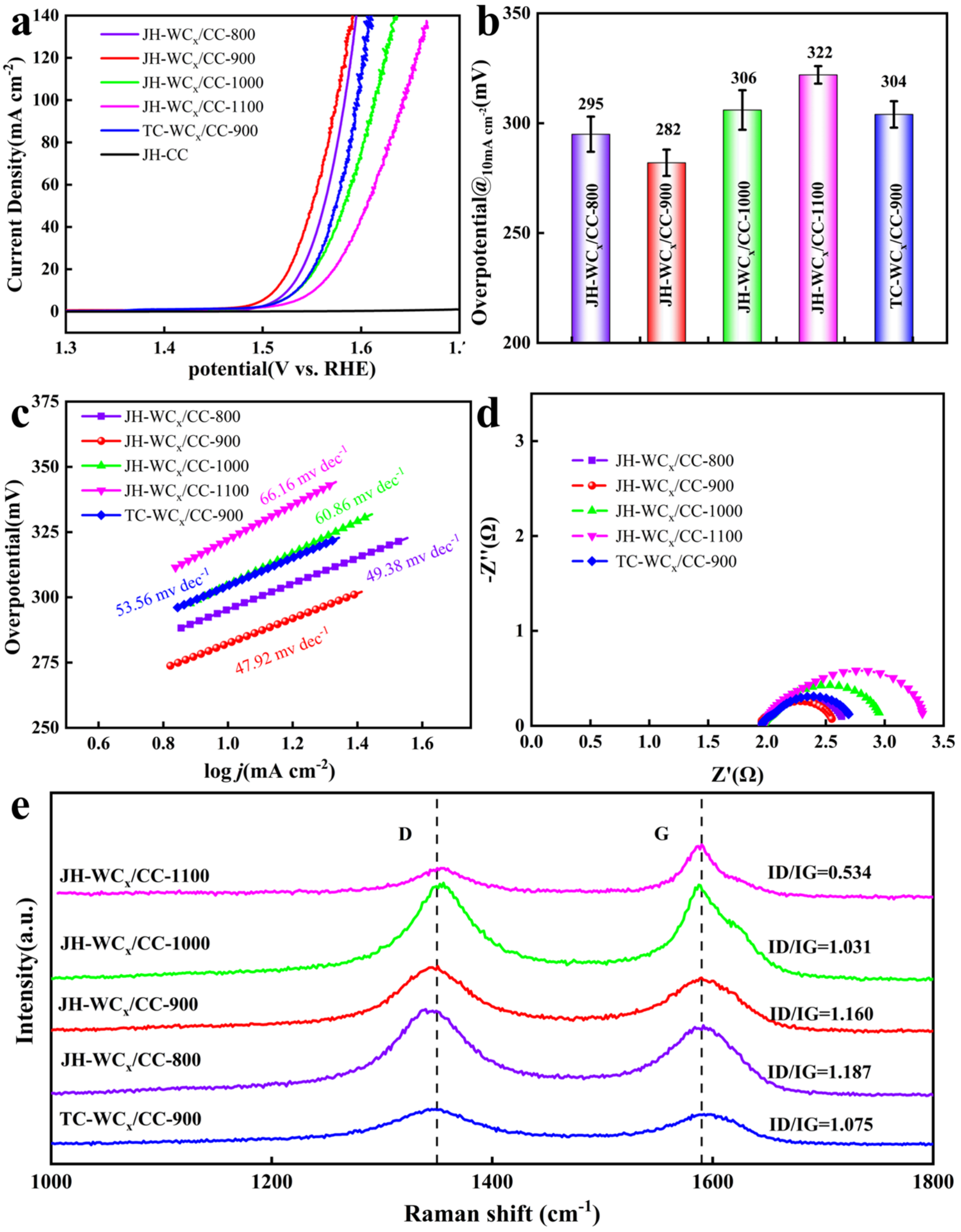

Figure 4. (a) LSV curves of the OER, (b) comparison of η_{10}, (c) Tafel slope diagram, (d) EIS Nyquist in 1 M KOH, and (e) Raman spectra of different patterns.

period of time,[26,27] avoiding agglomeration and growth of particles.

To analyze the phase composition of the samples after different heat treatments, XRD tests were carried out and the results are shown in Figure 3. The X-ray diffraction patterns containing JH-CC, JH-WC$_x$/CC-900 and TC-WC$_x$/CC-900 are shown in Figure 3a. JH-CC has only an amorphous peak of carbon, and Joule-heated JH-WC$_x$/CC-900 has W_2C (PDF#35-0776) and WC (PDF#51-0939) as its main phases.

However, for TC-WC$_x$/CC-900 synthesized by conventional heat treatment under the same temperature conditions, the main phases were W (PDF#04-0806) and WO_3 (PDF#46-1096), and no carbide phase was generated. Since the main pathway of carbothermal reduction of WO_3 is $WO_3 \rightarrow W \rightarrow W_2C \rightarrow WC$, the main reaction can be described by eqs 1−3.[28−32]

$$2W + C = W_2C \tag{1}$$

$$W + C = WC \tag{2}$$

$$W_2C + C = 2WC \tag{3}$$

That is, at the same temperature, the Joule heating method is more conducive to the carbothermal reduction process than conventional sintering.

As illustrated in Figure 3b, the phase composition of the samples varies with the Joule heating temperature. At 800 °C, the main phases of JH-WC$_x$/CC are W and WO_3, and at 900 °C, the precursor begins to carbonize, resulting in the main phases of JH-WC$_x$/CC to be WC and W_2C, respectively. When the Joule heating temperatures are increased to 1000 and 1100 °C, the main phases change to the WC structure and no longer change, which is consistent with the above-mentioned carbon-reduction process for WO_3. This is

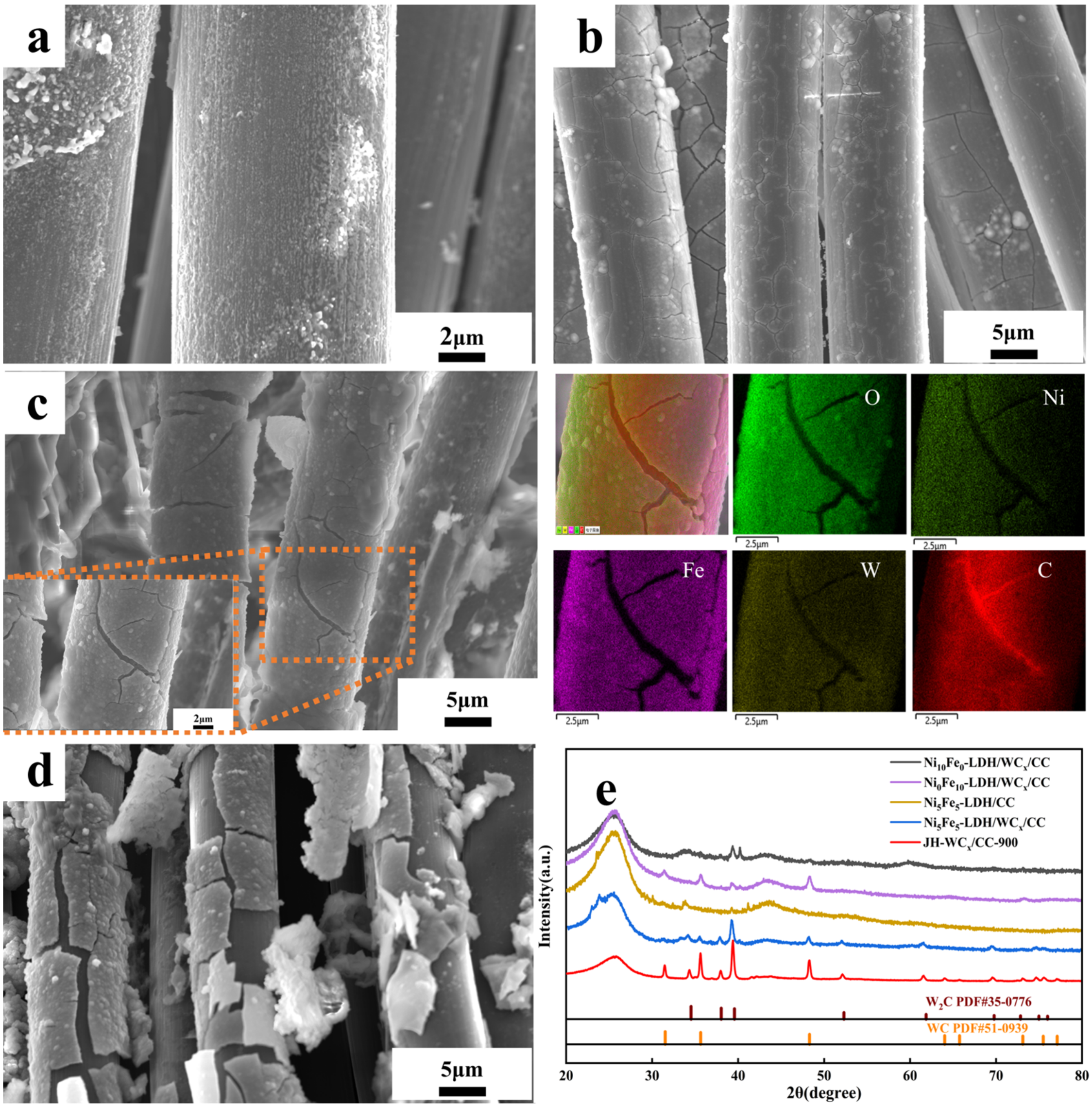

Figure 5. SEM images of Ni_yFe_{10-y}-LDH/WC_x/CC. (a) Ni_0Fe_{10}-LDH/WC_x/CC, (b) $Ni_{10}Fe_0$-LDH/WC_x/CC, (c) Ni_5Fe_5-LDH/WC_x/CC, (d) Ni_5Fe_5-LDH/CC without WC_x, and (e) X-ray diffraction patterns.

consistent with the carbonation reduction process of WO_3 described above.

To analyze the phase changes of tungsten precursors on carbon cloth, TG tests under a nitrogen atmosphere were conducted. The results of these tests are presented in Figure 3c. It was found that the mass of the sample and its decomposition rate did not change after 1000 °C. However, by comparison of the X-ray diffraction (XRD) spectra of the samples synthesized by Joule heating at different temperatures (Figure 3b), it was found that the phase compositions of the samples remained unchanged after 900 °C. This side-by-side reinforces the fact that Joule heating is an efficient way to prepare carbon by thermal reduction. In summary, it can be assumed that during the Joule-heated synthesis process, CC generates ultrarapid high-temperature thermal shocks under the action of Joule heat, which prompts the carbothermal reduction reaction, which does not easily occur in conventional heat treatment, to be realized under this condition, resulting in the in situ synthesis of WC_x on the CC carrier.

The prepared carbon cloth integrated electrode, which was directly used as the working electrode, was analyzed for its OER. The linear scanning voltammetric curve of the sample at a scan rate of 5 mV/s is presented in Figure 4a. In this paper, the electrocatalytic performance of Joule-heated products at different temperatures (900−1100 °C) was compared to determine the optimal conditions for the synthesis of WC_x/CC. These data have been *iR*-corrected (90%), and the LSV curves before and after the IR correction are shown in Figure S2.

As can be seen from Figure 4a,b, as the Joule heat treatment temperature increases, the value of the overpotential corresponding to 10 mA cm^{-2} also increases and then decreases, showing a minimal value of 282 mV at 900 °C. It was compared with the sample TC-WC_x/CC-900 calcined in a conventional tube furnace under a nitrogen atmosphere for 2 h. The catalytic activity of TC-WC_x/CC-900 (η_{10} = 304 mV) is worse than that of JH-WC_x/CC-900 prepared by Joule heating at the same temperature. This may be due to particle agglomeration caused by conventional sintering over a long period, which can significantly reduce the effective surface area of the material and hence its catalytic properties.[33,34] The pattern is consistent with the SEM results for the two sets of samples presented in Figure 2.

As demonstrated in Figure 4c, the corresponding Tafel slope initially increases and then decreases as the Joule heat treatment temperature rises. The Tafel slope reaches its minimum value (47.92 mV dec^{-1}) at 900 °C. The Tafel slope of TC-WC_x/CC-900 (53.56 mV dec^{-1}) is significantly higher than that of JH-WC_x/CC-900, which was prepared by Joule heating at the same temperature when compared with the TC-WC_x/CC-900 samples calcined in a conventional tube furnace under nitrogen for 2 h. The Tafel slope of TC-WC_x/CC-900 (53.56 mV dec^{-1}) is significantly higher than that of JH-WC_x/CC-900, which was prepared by Joule heating at the same temperature. This pattern is consistent with that of the overpotential.

As shown in Figure 4d, the EIS analysis investigated the charge transfer kinetics during the OER process, and the results were consistent with other measurements, indicating that JH-WC_x/CC-900 has the fastest electron transfer kinetics during the OER process, relative to the other catalysts. These results indicate that JH-WC_x/CC-900 has acceptable OER electrocatalytic performance. And by the C_{dl} values obtained from CV scans at different sweep speeds (Figure S4), it can be seen that JH-WC_x/CC-900 has an acceptable C_{dl} value, indicating that it has an acceptable number of active sites.

In addition, the type of heat treatment and the temperature affect the corresponding carbon defects and the degree of graphitization, leading to differences in catalytic properties. Raman characterization was carried out for this purpose and is shown in Figure 4e. The D peak is located near 1350 cm^{-1} and the G peak is located at 1580 cm^{-1}, the ratio of peak intensity between the D and G peaks represents the degree of carbon defects and the degree of graphitization of the material. The larger the ID/IG value, the more defects in the material, and the higher the degree of disorder, and on the contrary, the smaller the ID/IG value, the more ordered the material is, the higher the degree of graphitization.[35,36] Under the condition of Joule heating and holding for the same time, the ratio of ID/IG decreases with the increase of Joule heating temperature, which indicates the enhancement of graphitization of the material. While comparing the two heat treatments at 900 °C, it was found that the ID/IG ratio of JH-WC_x/CC-900 was 1.16, which was higher than that of TC-WC_x/CC-900, i.e., the nonequilibrium ultrarapid shock process with Joule heat helps to create more defective structures, which is similar to the conclusion in the literature.[37] The higher ID/IG values of JH-WC_x/CC-900 indicate the presence of a higher density of defects that increase the adsorption capacity sites, which provide a greater number of catalytically active sites for OER compared to the TC-WC_x/CC-900 electrocatalyst.[38−40]

The better catalytic performance of JH-WC_x/CC-900 compared to other temperatures is because, on the one hand, compared to 800 °C, it is due to the existence of a two-phase heterostructure of WC and W_2C in JH-WC_x/CC-900, and this heterostructure induces the transfer and redistribution of electrons between WC and W_2C. In addition, as the temperature increases, the physical phase of the material remains unchanged, and the degree of graphitization on the CC surface is enhanced, which means that the higher the temperature, the less the degree of carbon defects, and the more defects are conducive to the exposure of active sites and the increase of intrinsic activity.[41−43] In the latest findings, it is mentioned that there is a more favorable WC to W_2C ratio when heated at 900 °C using Joule heating and the synergistic effect of WC_x multiphase structure promotes the charge transfer.[44]

Subsequent studies have used prepared catalysts by rapid joule heat (JH-WC_x/CC-900) as the research basis material.

3.2. OER Study of NiFe-LDH/WC_x/CC.

To further enhance the OER performance of the catalyst, the surface of JH-WC_x particles were covered with a layer of NiFe-LDH by electrochemical deposition. SEM and its EDS images of Ni_yFe_{10-y}-LDH/WC_x/CC obtained after surface electrodeposition of JH-WC_x/CC at 900 °C are shown in Figure 5a−c. Figure 5a shows the shape of Ni_yFe_{10-y}-LDH/WC_x/CC (y = 0), which shows that iron hydroxide alone deposited on the surface of JH-WC_x/CC does not encapsulate the WC_x/CC and there is a nonuniform distribution of granular material. Figure 5c shows the SEM plot of Ni_yFe_{10-y}-LDH/WC_x/CC (y = 5), Ni_5Fe_5-LDH forms a layer outside of JH-WC_x/CC-900, and the erection of such a cladding structure is favorable for the exposure of electrocatalytic active sites and their rapid electron transfer. The EDS spectrum shows that Ni, Fe, and O are uniformly distributed on the external surface of JH-WC_x/CC-900, which is consistent with the XRD results. Figure 5d shows Ni_yFe_{10-y}-LDH/WC_x/CC (y = 10), and it can be seen that $Ni_{10}Fe_0$-LDH deposited on the $Ni_{10}Fe_0$-LDH/WC_x/CC surface completely encapsulates WC_x/CC. As shown in Figure 5d, the SEM image of Ni_5Fe_5-LDH/CC obtained after electrodeposition on the surface of empty carbon cloth JH-CC without the presence of carbide particles, it can be seen that a large amount of Ni_5Fe_5-LDH layer deposited on the surface is detached, and the bonding of the deposited layer to the substrate is weaker, which leads to disadvantages of its catalytically active sites, such as reduced electron transport and reduced stability.

As shown in Figure S6, the TEM and EDS spectra of Ni_5Fe_5-LDH/WC_x/CC can be seen in the high-resolution TEM image, and it can be seen that there are WC, W_2C, WO_3, and some amorphous Ni_5Fe_5-LDH on the surface, among which 0.376 nm corresponds to the (2 0 0) crystal plane of WO_3,[45] 0.283 nm corresponds to the (0 0 1) crystal plane of WC,[12] and 0.259 nm corresponds to the (1 0 0) crystal plane of W_2C.[24] This indicates that the catalyst contains WC and W_2C, as well as a small amount of WO_3 due to the oxidation of the surface in contact with air. From its EDS spectra, it can be seen that the Ni, Fe, W, C, and O elements on the surface of the catalyst are evenly distributed and the atomic ratio of Ni/Fe is 1.17.

The X-ray diffractogram of Ni_yFe_{10-y}-LDH/WC_x/CC synthesized by electrodeposition is shown in Figure 5e. It can be seen that the diffraction peaks of Ni_5Fe_5-LDH/WC_x/CC correspond to the diffraction peaks of WC (PDF#51-0939) and W_2C (PDF#35-0776), which proves that Ni_5Fe_5-LDH/WC_x/CC is an amorphous complex of NiFe-LDH, WC, and W_2C.

The electrocatalytic performance of the prepared electrodes was investigated within a typical three-electrode system in a 1 M KOH electrolyte. Electrochemical scanning was conducted in reverse direction at a scan rate of 5 mV/s to obtain the LSV curves of the integrated electrode materials of Ni_yFe_{10-y}-LDH/WC_x/CC in different ratios and Ni_5Fe_5-LDH/CC without tungsten carbide alone. These data were 90% *iR*-corrected, and the LSV curves before and after IR compensation are shown in

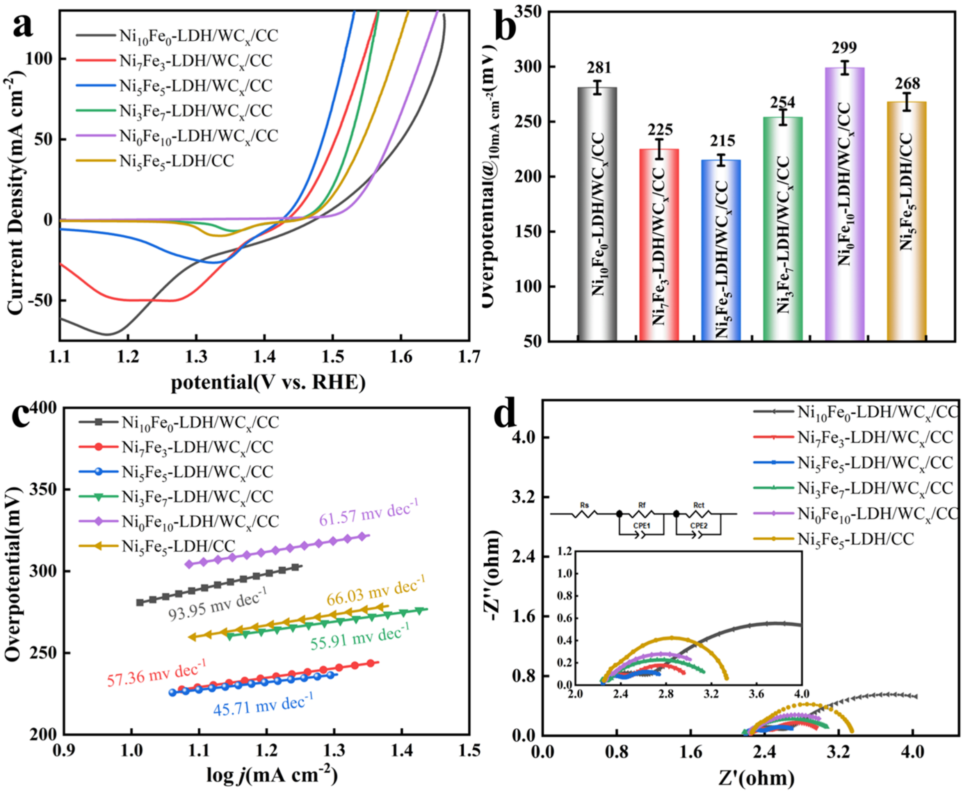

Figure 6. (a) LSV curves of Ni_yFe_{10-y}-LDH/WC_x/CC, (b) comparison of η_{10}, (c) Tafel plots, and (d) EIS Nyquist.

Figure S5. As can be seen in Figure 6a, the performance of Ni_yFe_{10-y}-LDH/WC_x/CC increases as the Ni/Fe ratio increases, but too high a ratio also leads to an effect on the performance, with the best overpotential for Ni_5Fe_5-LDH/WC_x-CC being reached at $y = 5$ ($\eta_{10} = 215$ mV). This enhancement emphasizes the positive impact of introducing iron into the material, thus improving the catalytic performance. This is consistent with the beneficial role of Fe^{3+} in Ni^{2+}-containing LDH materials highlighted by researchers, where iron plays a crucial role in regulating layer spacing and increasing conductivity.[46−50] It is worth noting that, unlike Ni, Fe itself does not participate in redox reactions in the OER.[51] Although NiFe-LDH is considered to be a suitable material for catalyzing OER,[52] it can be determined from Figure 6b that the performance of Ni_5Fe_5-LDH/WC_x/CC ($\eta_{10} = 215$ mV) is much better than that of JH-WC_x/CC-900 ($\eta_{10} = 282$ mV) and Ni_5Fe_5-LDH/CC ($\eta_{10} = 268$ mV). In the alkaline OER process, the adsorption of reaction intermediates on the electrode surface has an important influence on the OER performance.[53] Since the surface active sites of NiFe-LDH have a strong adsorption capacity for hydroxyl radicals[54] and the poor conductivity of NiFe-LDH can be improved by utilizing the high electronic conductivity of WC_x/CC,[55] Ni_5Fe_5-LDH/WC_x/CC can rapidly oxidize hydroxyl radicals to a variety of reaction intermediates, accelerating the electron transfer between electrodes. In addition, due to the synergistic coupling between both NiFe-LDH and WC_x as well as the advantages of the cladding structures,[56] the catalytic performance of NiFe-LDH/WC_x/CC is greatly improved. As shown in Table S2, the performance of Ni_5Fe_5-LDH/WC_x/CC is compared with other representative catalysts of the OER in 1 M KOH solution, which shows that Ni_5Fe_5-LDH/WC_x/CC has excellent electrocatalytic performance.

Tafel was used to evaluate the reaction kinetics of the OER catalyst samples. The Tafel curves of Ni_yFe_{10-y}-LDH/WC_x/CC electrode materials at different ratios are shown in Figure 6c. The Tafel slope for Ni_5Fe_5-LDH/WC_x/CC is much lower (45.71 mV dec^{-1}). Ni_5Fe_5-LDH/WC_x/CC catalysts exhibited faster reaction kinetics and demonstrated an efficient OER performance.

The kinetics of OER catalysts were further evaluated using EIS. The EIS of Ni_yFe_{10-y}-LDH/WC_x/CC electrode materials at different ratios are shown in Figure 6d. It can be seen that these EIS curves appear as double semicircles. It is due to interfacial synergism, where heterogeneous interfaces of LDH and WC_x may form different charge transfer pathways. Arcing in the high-frequency region usually corresponds to the charge transfer resistance at the catalyst/electrolyte interface, whereas arcing in the low-frequency region may be due to the presence of some WO_3 in the material, resulting in impeded charge transfer. For example, a similar situation was observed in the study of Abedi et al.[56] As demonstrated in Figure S3, the bore plot of Ni_5Fe_5-LDH/WC_x/CC. The smaller the diameter of the semicircle in the impedance spectrum, the smaller the charge transfer resistance (R_{ct}) value. The smaller the semicircle, the smaller the R_{ct}. It can be seen that the R_{ct} of Ni_5Fe_5-LDH/WC_x/CC electrocatalysts is much smaller than that of NiFe-LDH/CC electrocatalysts, suggesting that Ni_5Fe_5-LDH/WC_x/CC has a faster charge transfer rate. And by the C_{dl} values obtained from CV scans at different sweep speeds (Figure S7), it can be seen that Ni_5Fe_5-LDH/WC_x/CC has an acceptable C_{dl} value, indicating that it has an acceptable number of active sites.

To demonstrate the potential for long-term applications, we tested the long-term cycling stability of Ni_5Fe_5-LDH/WC_x/CC. As shown in Figure S8, Ni_5Fe_5-LDH/WC_x/CC maintains

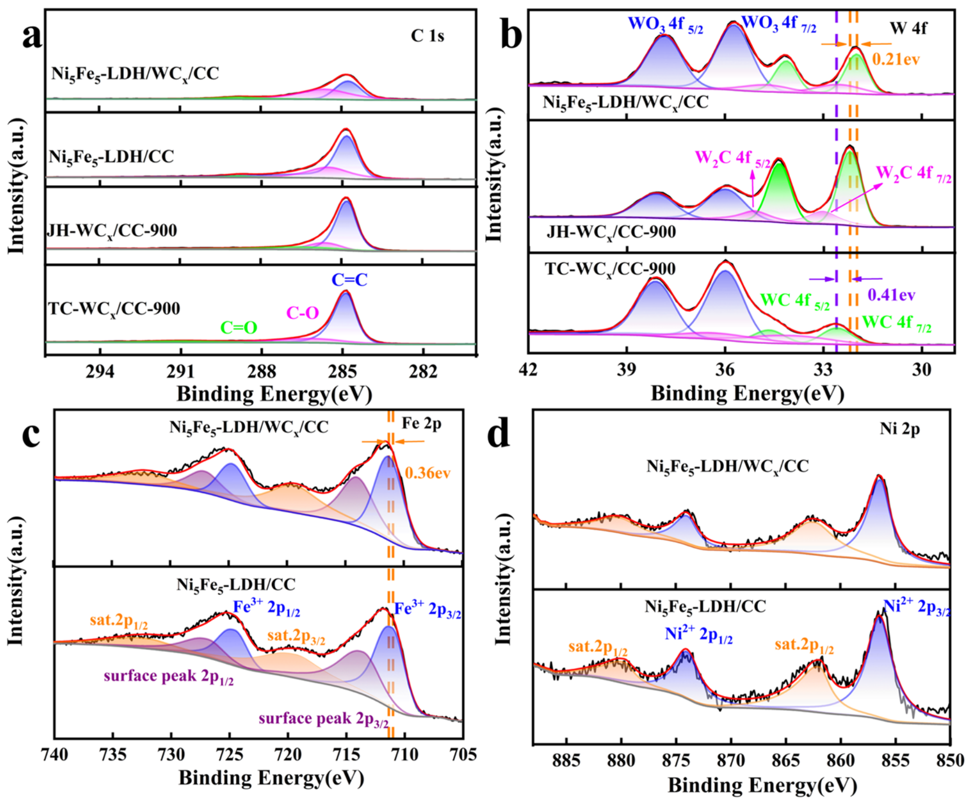

Figure 7. XPS test spectra of samples TC-WC_x/CC-900, JH-WC_x/CC-900, Ni_5Fe_5-LDH/CC, and Ni_5Fe_5-LDH/WC_x/CC. (a) C 1s, (b) W 4f, (c) Fe 2p, and (d) Ni 2p.

90.6% of the current density at a current density of 10 mA cm^{-2} for a long period of 25 h. The phase structure after the long-term stability test is shown in S10, which shows that the structure of WC_x has not changed but its crystallinity has decreased. In addition, the metal ion content in the solution after the ICP-MS test contains 0.0001 wt % of Ni, 0.0005 wt % of Fe, and 0.0038 wt % of W (Table S1), so the OER performance is slightly decreased after 25 h of testing.

The XPS survey spectrum (Figure S9) shows the presence of Ni, Fe, W, C, and O elements in Ni_5Fe_5-LDH/WC_x/CC, which is consistent with the EDS results.For Ni_5Fe_5-LDH/WC_x/CC, the C 1s profile consists of three distinct peaks at 284.8, 285.66, and 286.69 eV, corresponding to C═C, C−O, and C═O, respectively (Figure 7a). For W 4f, there are three pairs of peaks. The first pair of peaks with the lowest binding energies (31.98 eV for W $4f_{7/2}$ and 34.12 eV for W $4f_{5/2}$) can be attributed to W^{4+} in WC.[57] The second pair of peaks (32.54 eV for W $4f_{7/2}$ and 34.75 eV for W $4f_{5/2}$) can be attributed to W^{2+} in W_2C.[58] The third pair of peaks with the highest binding energies (35.73 eV for W $4f_{7/2}$ and 37.84 eV for W $4f_{5/2}$) can be attributed to WO_3 due to the unavoidable oxidization of WC nanoparticles when exposed to air.[23] (Figure 7b) In the Fe 2p spectra, the binding energies of 711.37, 724.77, 714.08, 727.18, 719.49, and 732.29 eV belong to Fe^{3+} $2p_{3/2}$, Fe^{3+} $2p_{1/2}$, surface peak $2p_{3/2}$, surface peak $2p_{1/2}$, characteristic peak sat.$2p_{3/2}$, and characteristic peak sat.$2p_{1/2}$, respectively (Figure 7c), which indicating that the Fe atoms in Ni_5Fe_5-LDH/WC_x/CC are +3 valence.[59,60] In the Ni 2p spectra, the peaks at 856.36, 873.95, 862.40, and 880.11 eV correspond to Ni^{2+} $2p_{3/2}$, Ni^{2+} $2p_{3/2}$, the characteristic peak sat.$2p_{1/2}$, and the characteristic peak sat.$2p_{3/2}$, respectively (Figure 7d), which suggests that the Ni atoms in Ni_5Fe_5-LDH/WC_x/CC are +2 valence.[61−63]

As shown in Figure 6c, the binding energy of JH-WC_x/CC-900 is reduced by 0.41 eV compared with that of W 4f of TC-WC_x/CC-900, which may be related to the carbon defects induced by the rapid temperature rise and fall during Joule heating.[64]

We can see that Ni_5Fe_5-LDH/WC_x/CC is negatively displaced, and the binding energy is reduced by 0.21 eV compared to W 4f in JH-WC_x/CC-900, i.e., electrons are gained by the electron transfer process that occurs after the formation of the heterostructure (Figure 7b). The binding energies of Ni_5Fe_5-LDH/WC_x/CC were reduced by 0.11 eV compared to Ni 2p in Ni_5Fe_5-LDH/CC, respectively (Figure 7d). In contrast, Ni_5Fe_5-LDH/WC_x/CC showed an increase in the binding energy of 0.31 eV compared to Fe 2p in Ni_5Fe_5-LDH/CC (Figure 7c). These changes in the binding energies of W 4f, Ni 2p, and Fe 2p indicate that they suggest electronic interactions between these two components. Moreover, when Ni_5Fe_5-LDH is introduced, the electrons around the Ni and W atoms are enriched, and the electrons around the Fe atoms are depleted, suggesting that the electrons migrate from Fe to W and Ni. This electron transfer ultimately contributes to the enhancement of the intrinsic activity of the electrocatalytic oxygen precipitation reaction.[65]

That is, in the material Ni_5Fe_5-LDH/WC_x/CC, the Fe 2p peak is positively shifted by 0.31 eV, while the W 4f peak and the Ni 2p peak are negatively shifted by 0.21 and 0.11 eV, respectively. This suggests that the charge transfer from Fe to W and Ni occurs in the Ni_5Fe_5-LDH/WC_x/CC material, and this charge transfer results in the Fe, W, and Ni nuclear energy level shifts in opposite directions,[66−68] thereby greatly stimulating the synergistic interaction of Ni_5Fe_5-LDH with WC_x.

4. CONCLUSIONS

In summary, we have successfully synthesized highly dispersed nanoparticles of WC_x in situ on carbon cloth by carbothermal reduction at high temperatures using a fast Joule heating method. The optimum synthesis temperature of 900 °C was verified by electrochemical testing of the catalysts at different temperatures. Moreover, the electrochemical performance of JH-WC_x/CC-900 is better than that of TC-WC_x/CC-900. The results of SEM and Raman spectroscopy show that Joule heating avoids the problems of particle agglomeration and a low degree of carbon defects that are caused by prolonged sintering in conventional sintering.

The successful synthesis of a layer of NiFe-LDH was achieved through the process of electrodeposition on the surface of JH-WC_x/CC-900. Furthermore, Ni_5Fe_5-LDH/WC_x/CC exhibited a remarkably low overpotential value of 215 mV, along with a notable durability. In addition, the catalyst has the advantages of low impedance, fast electron transfer rate, low slope of the Tafel curve, and fast reaction kinetics performance. This excellent performance may be attributed to the synergistic effect between different components of the heterogeneous structure as well as the advantages of the encapsulated structure.

■ ASSOCIATED CONTENT

Supporting Information

The Supporting Information is available free of charge at https://pubs.acs.org/doi/10.1021/acsaem.5c00500.

> EDS plots for JH-WC_x/CC-900 and TC-WC_x/CC-900; LSV curves of WC_x/CC and Ni_yFe_{10-y}-LDH/WC_x/CC catalysts before and after *iR* correction; Bode plot of Ni_5Fe_5-LDH/WC_x/CC; C_{dl} and CV plots of WC_x/CC and Ni_yFe_{10-y}-LDH/WC_x/CC; TEM and EDS images of Ni_5Fe_5-LDH/WC_x/CC; stability plot of Ni_5Fe_5-LDH/WC_x/CC; the XPS survey spectrum; XRD plots before and after stability test; percentage of metal ions in ICP-MS test solution; comparison of the performance of Ni_5Fe_5-LDH/WC_x/CC with other representative catalysts. (PDF)

■ AUTHOR INFORMATION

Corresponding Author

Lili Guan – *School of Materials Science and Engineering, Inner Mongolia University of Science and Technology, Baotou 014010, China*; orcid.org/0000-0002-9278-410X; Email: guanlili907007@163.com

Authors

Pengchong Shen – *School of Materials Science and Engineering, Inner Mongolia University of Science and Technology, Baotou 014010, China*

Zhekai Zhang – *School of Chemistry and Chemical Engineering, Harbin Institute of Technology, Harbin 150001 Heilongjiang, China*

Jiaming Zhao – *School of Materials Science and Engineering, Inner Mongolia University of Science and Technology, Baotou 014010, China*

Yaqi Yang – *School of Materials Science and Engineering, Inner Mongolia University of Science and Technology, Baotou 014010, China*

Li Wu – *School of Materials Science and Engineering, Inner Mongolia University of Science and Technology, Baotou 014010, China*

Yarong Huang – *School of Materials Science and Engineering, Inner Mongolia University of Science and Technology, Baotou 014010, China*

Menggang Li – *School of Chemistry and Chemical Engineering, Harbin Institute of Technology, Harbin 150001 Heilongjiang, China*

Xiwen Song – *School of Materials Science and Engineering, Inner Mongolia University of Science and Technology, Baotou 014010, China*

Complete contact information is available at: https://pubs.acs.org/10.1021/acsaem.5c00500

Notes

The authors declare no competing financial interest.

■ ACKNOWLEDGMENTS

The project is supported by the National Natural Science Foundation of China (52162010, 52372062), the Inner Mongolia Autonomous Region Natural Science Foundation Program (2024MS05037), and First-Class Discipline Research Special Project of Inner Mongolia Autonomous Region Department of Education (YLXKZX-NKD-032).

■ REFERENCES

(1) Wang, X.; Zhong, H.; Xi, S.; et al. Understanding of Oxygen Redox in the Oxygen Evolution Reaction. *Adv. Mater.* **2022**, *34* (50), No. 2107956.

(2) Du, Y.; Cheng, G.; Luo, W. Colloidal Synthesis of Urchin-Like Fe Doped $NiSe_2$ for Efficient Oxygen Evolution. *Nanoscale* **2017**, *9* (20), 6821−6825.

(3) Li, Z.; Liu, D.; Lu, X.; et al. Boosting Oxygen Evolution of Layered Double Hydroxide Through Electronic Coupling with Ultralow Noble Metal Doping. *Dalton Trans.* **2022**, *51* (4), 1527−1532.

(4) Wang, Z.; Xiao, B.; Lin, Z.; et al. In-Situ Surface Decoration of Ruo_2 Nanoparticles by Laser Ablation for Improved Oxygen Evolution Reaction Activity in Both Acid and Alkali Solutions. *J. Energy Chem.* **2021**, *54*, 510−518.

(5) Tamilarasi, B.; Jithul, K. P.; Pandey, J. Non-Noble Metal-Based Electro-Catalyst for the Oxygen Evolution Reaction (OER): Towards an Active & Stable Electro-Catalyst for PEM Water Electrolysis. *Int. J. Hydrogen Energy* **2024**, *58*, 556−582.

(6) Huang, Y.; Liu, L.; Liu, X. Modulated Electrochemical Oxygen Evolution Catalyzed by MoS_2 Nanoflakes from Atomic Layer Deposition. *Nanotechnology* **2019**, *30* (9), No. 095402.

(7) Liu, J.; Zhao, S.; Li, C.; et al. Carbon Nanodot Surface Modifications Initiate Highly Efficient, Stable Catalysts for both Oxygen Evolution and Reduction Reactions. *Adv. Energy Mater.* **2016**, *6* (9), No. 1502039.

(8) Ede, S. R.; Luo, Z. Tuning the Intrinsic Catalytic Activities of Oxygen-Evolution Catalysts by Doping: a Comprehensive Review. *J. Mater. Chem. A* **2021**, *9* (36), 20131−20163.

(9) Diao, J.; Qiu, Y.; Liu, S.; et al. Interfacial Engineering of W_2N/WC Heterostructures Derived from Solid-State Synthesis: A Highly Efficient Trifunctional Electrocatalyst for ORR, OER, and HER. *Adv. Mater.* **2020**, *32* (7), No. 1905679.

(10) Das, D.; Santra, S.; Nanda, K. K. In Situ Fabrication of a Nickel/Molybdenum Carbide-Anchored N-Doped Graphene/CNT

Hybrid: An Efficient (Pre) Catalyst for OER And HER. *ACS Appl. Mater. Interfaces* **2018**, *10* (41), 35025−35038.

(11) Wang, B.; Ai, Y.; Yao, Y.; et al. Electrochemical Synergy Between FeNi Nanoalloy@Tungsten Carbide on N-Doped Graphitized Carbon Layers as an Excellent Electrocatalyst for Oxygen Evolution Reaction. *Electrochim. Acta* **2022**, *415*, No. 140254.

(12) Ren, G.; Hu, J.; Wang, K.; et al. Synergistically Coupling of WC-WP/NC Hybrid Catalyst for Electrocatalytic Hydrogen Production. *J. Electroanal. Chem.* **2023**, *932*, No. 117216.

(13) Chen, Y.; Egan, G. C.; Wan, J.; et al. Ultra-Fast Self-Assembly and Stabilization of Reactive Nanoparticles in Reduced Graphene Oxide Films. *Nat. Commun.* **2016**, *7* (1), No. 12332.

(14) Yang, C.; Yao, Y.; He, S.; et al. Ultrafine Silver Nanoparticles for Seeded Lithium Deposition toward Stable Lithium Metal Anode. *Adv. Mater.* **2017**, *29* (38), No. 1702714.

(15) Chen, Y.; Li, Y.; Wang, Y.; et al. Rapid. In Situ Synthesis of High Capacity Battery Anodes Through High Temperature Radiation-Based Thermal Shock. *Nano Lett.* **2016**, *16* (9), 5553−5558.

(16) Yao, Y.; Huang, Z.; Xie, P.; et al. Ultrafast, Controllable Synthesis of Sub-Nano Metallic Clusters Through Defect Engineering. *ACS Appl. Mater. Interfaces* **2019**, *11* (33), 29773−29779.

(17) Xie, H.; Fu, K.; Yang, C.; et al. Necklace-Like Silicon Carbide and Carbon Nanocomposites Formed by Steady Joule Heating. *Small Methods* **2018**, *2* (4), No. 1700371.

(18) Chen, Y.; Xu, S.; Li, Y.; et al. FeS_2 Nanoparticles Embedded in Reduced Graphene Oxide toward Robust, High-Performance Electrocatalysts. *Adv. Energy Mater.* **2017**, *7* (19), No. 1700482.

(19) Chen, Y.; Xu, S.; Zhu, S.; et al. Millisecond Synthesis of CoS Nanoparticles For Highly Efficient Overall Water Splitting. *Nano Res.* **2019**, *12*, 2259−2267.

(20) Xu, S.; Chen, Y.; Li, Y.; et al. Universal, in Situ Transformation of Bulky Compounds into Nanoscale Catalysts by High-Temperature Pulse. *Nano Lett.* **2017**, *17* (9), 5817−5822.

(21) Yao, Y.; Huang, Z.; Xie, P.; et al. Carbothermal Shock Synthesis of High-Entropy-Alloy Nanoparticles. *Science* **2018**, *359* (6383), 1489−1494.

(22) Xie, P.; Yao, Y.; Huang, Z.; et al. Highly Efficient Decomposition of Ammonia Using High-Entropy Alloy Catalysts. *Nat. Commun.* **2019**, *10* (1), No. 4011.

(23) Ma, Y.-Y.; Lang, Z.; Yan, L.; et al. Highly Efficient Hydrogen Evolution Triggered by a Multi-Interfacial Ni/WC Hybrid Electrocatalyst. *Energy Environ. Sci.* **2018**, *11* (8), 2114−2123.

(24) Chen, Z.; Gong, W.; Cong, S.; et al. Eutectoid-Structured WC/W_2C Heterostructures: A New Platform for Long-Term Alkaline Hydrogen Evolution Reaction at Low Overpotentials. *Nano Energy* **2020**, *68*, No. 104335.

(25) Zhu, Y.; Guan, L.; Song, X.; et al. Regulation of Surface Oxygen Vacancy of Cu-CeO_2/TiO_2 Heterostructures via Fast Joule Heating Method for Enhanced CO_2 Electrochemical Reduction. *J. Alloys Compd.* **2024**, *1006*, No. 176198.

(26) Yao, Y.; Chen, F.; Nie, A.; et al. In Situ High Temperature Synthesis of Single-Component Metallic Nanoparticles. *ACS Cent. Sci.* **2017**, *3* (4), 294−301.

(27) Chen, F.; Yao, Y.; Nie, A.; et al. High-Temperature Atomic Mixing toward Well-Dispersed Bimetallic Electrocatalysts. *Adv. Energy Mater.* **2018**, *8* (25), 1800466.

(28) Wu, H.; Wang, Q.; Qin, M.; et al. Synthesis of Tungsten Carbide Nanopowders by Direct Carbonization of Tungsten Oxide and Carbon: Effects of Tungsten Oxide Source on Phase Structure and Morphology Evolution. *Ceram. Int.* **2020**, *46* (7), 8787−8795.

(29) Deng, X.-C.; Kang, X.; Cui, J.; Zhang, G. H. Reaction Mechanism and Kinetics of Carbothermal Reduction of WO_3 to Produce WC. *JOM* **2023**, *75* (3), 872−885.

(30) Wang, Q.; Wu, H.; Qin, M.; et al. Study on Influencing Factors and Mechanism of High-Quality Tungsten Carbide Nanopowders Synthesized via Carbothermal Reduction. *J. Alloys Compd.* **2021**, *867*, No. 158959.

(31) Stanciu, V. I.; Vitry, V.; Delaunois, F. Tungsten Carbide Powder Obtained by Direct Carburization of Tungsten Trioxide Using Mechanical Alloying Method. *J. Alloys Compd.* **2016**, *659*, 302−308.

(32) Liu, B.; Shi, A.; Yang, G.; et al. Recovery of Tungsten Carbides for Preparing Ultrafine WC-Co Composite Powder Using Core-Shell Structured Precursor Synthesized by CVD. *Int. J. Refract. Met. Hard Mater.* **2017**, *67*, 74−81.

(33) Lee, C. S.; Gong, J.; Huong, C. V. Macroporous Alginate Substrate-Bound Growth of Fe^0 Nanoparticles With High Redox Activities or Nitrate Removal from Aqueous Solutions. *Chem. Eng. J.* **2016**, *298*, 206−213.

(34) Reinders, N.; Durovic, M.; Honcova, P.; et al. High-Temperature Preparation of Ni_2P Suspended Within Carbon Matrix and Its Potential As HER Electrocatalyst. *Microporous Mesoporous Mater.* **2024**, *364*, No. 112870.

(35) Selepe, C. T.; Gwebu, S. S.; Matthews, T.; et al. Effect of Sn Doping on Pd Electro-Catalysts for Enhanced Electro-Catalytic Activity towards Methanol and Ethanol Electro-Oxidation in Direct Alcohol Fuel Cells. *Nanomaterials* **2021**, *11* (10), 2725.

(36) Miao, J.; Zhao, X.; Hu, H.; Liu, Z. H. Hierarchical Ultrathin Nife-Borate Layered Double Hydroxide Nanosheets Encapsulated into Biomass-Derived Nitrogen-Doped Carbon for Efficient Electrocatalytic Oxygen Evolution. *Colloids Surf., A* **2022**, *635*, No. 128092.

(37) Liao, Y.; Zhu, R.; Zhang, W.; et al. Transient Synthesis of Carbon-Supported High-Entropy Alloy Sulfide Nanoparticles via Flash Joule Heating for Efficient Electrocatalytic Hydrogen Evolution. *Nano Res.* **2024**, *17* (4), 3379−3389.

(38) Lin, X.; Liu, J.; Wu, L.; et al. In Situ Coupling of Lignin-Derived Carbon-Encapsulated CoFe-Co_xN Heterojunction for Oxygen Evolution Reaction. *AIChE J.* **2022**, *68* (10), No. e17785.

(39) Abu Hatab, A. S.; Ahmad, Y. H.; Ibrahim, M.; et al. MOF-Derived Cobalt@Mesoporous Carbon as Electrocatalysts for Oxygen Evolution Reaction: Impact of Organic Linker. *Langmuir* **2023**, *39* (3), 1123−1134.

(40) Cao, H.; Li, H.; Liu, L.; et al. Salt-Templated Nanoarchitectonics of $CoSe_2$-NC Nanosheets as an Efficient Bifunctional Oxygen Electrocatalyst for Water Splitting. *Int. J. Mol. Sci.* **2022**, *23* (9), 5239.

(41) Wei, P.; Li, X.; He, Z. Porous N, B Co-doped Carbon Nanotubes as Efficient Metal-Free Electrocatalysts for ORR and Zn-Air Batteries. *Chem. Eng. J.* **2021**, *422*, No. 130134.

(42) Lu, C.; Zhang, J.; Chen, Z.; et al. A Room-Temperature Interfacial Approach towards Iron/Nitrogen Co-Doped Fibrous Porous Carbons as Electrocatalysts for the Oxygen Reduction Reaction and Zn-Air Batteries. *Nanoscale* **2019**, *11* (21), 10257−10265.

(43) Gao, T.; Yu, S.; Chen, Y.; et al. Regulating the Thickness of the Carbon Coating Layer in Iron/Carbon Heterostructures to Enhance the Catalytic Performance for Oxygen Evolution Reaction. *J. Colloid Interface Sci.* **2023**, *642*, 120−128.

(44) Mashhadian, A.; Wu, S.; Hwang, T.; et al. Rapid Synthesis of Phase-Engineered Tungsten Carbide Electrocatalysts via Flash Joule Heating for High-Current-Density Hydrogen Evolution. *Int. J. Hydrogen Energy* **2025**, *106*, 973−979.

(45) Wang, B.; Fang, R.; Chen, K.; et al. Heterostructured WO_x/W_2C Nanocatalyst for Li_2S Oxidation in Lithium-Sulfur Batteries with High-Areal-Capacity. *Small* **2024**, *20* (27), No. 231081.

(46) Wang, Y.; Wang, X.; Min, Y.; et al. Investigation of Oxygen Evolution Performance of Highly Efficient Water Electrolysis Catalyst: NiFe LDH/BPene. *Processes* **2023**, *11* (7), 2179.

(47) Gicha, B. B.; Tufa, L. T.; Choi, Y.; Lee, J. Amorphous $Ni_{1-x}Fe_x$ Oxyhydroxide Nanosheets with Integrated Bulk and Surface Iron for a High and Stable Oxygen Evolution Reaction. *ACS Appl. Energy Mater.* **2021**, *4* (7), 6833−6841.

(48) Xu, H.; Liu, B.; Liu, J.; et al. Revealing the Surface Structure-Performance Relationship of Interface-Engineered NiFe Alloys for Oxygen Evolution Reaction. *J. Colloid Interface Sci.* **2022**, *622*, 986−994.

https://doi.org/10.1021/acsaem.5c00500
ACS Appl. Energy Mater. XXXX, XXX, XXX−XXX

(49) Wu, X.; Yang, F.; Shen, G. NiFe Single Atom Catalysts Anchored on Carbon for Oxygen Evolution Reaction. *Int. J. Hydrogen Energy* **2022**, *47* (44), 18955−18962.

(50) Lee, W. S.; Maeda, H.; Kuo, Y. T.; et al. Spontaneous-Spin-Polarized 2D π-d Conjugated Frameworks Towards Enhanced Oxygen Evolution Kinetics. *Small* **2024**, *20* (40), No. 2401987.

(51) Liu, W.; Gao, Y.; Wang, L.; Gong, Y. Fe^{3+} Induced Etching of NiCo-MOF Derived Transformations into Layered Ternary Hydroxides as Efficient Oxygen Evolution Catalyst. *Int. J. Hydrogen Energy* **2024**, *51*, 1229−1239.

(52) Zhou, L.; Zhang, C.; Zhang, Y.; et al. Host Modification of Layered Double Hydroxide Electrocatalyst to Boost the Thermodynamic and Kinetic Activity of Oxygen Evolution Reaction. *Adv. Funct. Mater.* **2021**, *31* (15), No. 2009743.

(53) Ma, L.; Zhang, M.; Peng, K.; et al. Single-and Double-Atom Catalyst Anchored on Graphene-Like C_2N for ORR and OER: Mechanistic Insight and Catalyst Screening. *Carbon Lett.* **2024**, *34* (5), 1367−1383.

(54) Zhou, S.; He, H.; Li, J.; et al. Regulating the Band Structure of Ni Active Sites in Few-Layered NiFe-LDH by in Situ Adsorbed Borate for Ampere-Level Oxygen Evolution. *Adv. Funct. Mater.* **2024**, *34* (12), No. 2313770.

(55) Zeng, M.; Luo, R.; Deng, X.; et al. Molten-Salt-Chemistry-Assisted Synthesis of Layered N-Doped Tungsten Carbide with Enhanced Electrical Conductivity for Efficient Electrocatalytic Hydrogen Evolution. *Int. J. Hydrogen Energy* **2024**, *92*, 1021−1029.

(56) Abedi, M.; Rezaee, S.; Shahrokhian, S. Designing Core-Shell Heterostructure Arrays based on Snowflake Nicofe-Lth Shelled over W_2N-WC Nanowires as an Advanced Bi-Functional Electrocatalyst for Boosting Alkaline Water/Seawater Electrolysis. *J. Colloid Interface Sci.* **2024**, *666*, 307−321.

(57) Yan, P.; Wu, Y.; Wei, X.; et al. Preparation of Robust Hydrogen Evolution Reaction Electrocatalyst WC/C by Molten Salt. *Nanomaterials* **2020**, *10* (9), 1621.

(58) Wang, B.; Fang, R.; Chen, K.; et al. Heterostructured WO_x/W_2C Nanocatalyst for Li_2S Oxidation in Lithium-Sulfur Batteries with High-Areal-Capacity. *Small* **2024**, *20* (27), No. 2310801.

(59) Wang, X.; Qin, Z.; Qian, J.; et al. FeNi-LDH Nanoflakes on Co-encapsulated CNT Networks for Stable and Efficient Ampere-Level Current Density Oxygen Evolution. *Appl. Catal., B* **2024**, *359*, No. 124506.

(60) Mullet, M.; Khare, V.; Ruby, C. XPS Study of Fe(II)-Fe(III) (oxy) hydroxycarbonate Green Rust Compounds. *Surf. Interface Anal.* **2008**, *40* (3−4), 323−328.

(61) He, J.; Zhou, X.; Xu, P.; Sun, J. Promoting Electrocatalytic Water Oxidation Through Tungsten-Modulated Oxygen Vacancies on Hierarchical FeNi-Layered Double Hydroxide. *Nano Energy* **2021**, *80*, No. 105540.

(62) Xiao, M.; Wu, C.; Zhu, J.; et al. In Situ Generated Layered NiFe-LDH/MOF Heterostructure Nanosheet Arrays with Abundant Defects for Efficient Alkaline and Seawater Oxidation. *Nano Res.* **2023**, *16* (7), 8945−8952.

(63) Wang, F.; Wang, T.; Sun, S.; et al. One-step Synthesis of Nickle Iron -layered Double Hydroxide/Reduced Graphene Oxide/Carbon Nanofibres Composite as Electrode Materials for Asymmetric Supercapacitor. *Sci. Rep.* **2018**, *8* (1), No. 8908.

(64) Son, J.; Choi, M.; Choi, H.; et al. Structural Evolution of Graphene in Air at the Electrical Breakdown Limit. *Carbon* **2016**, *99*, 466−471.

(65) Zhang, H.; Wang, J.; Zhang, Q.; et al. Regulating the Electronic State of Ni in an Alloy Phase by Heterogeneous Structures of $FeNi_3$-WC/C to Reach a High Performance for Oxygen Evolution Reaction. *J. Electrochem. Soc.* **2023**, *170* (1), No. 016505.

(66) Oh, S.; Kim, H.; Kwon, Y.; et al. Porous Co-P Foam as an Efficient Bifunctional Electrocatalyst for Hydrogen and Oxygen Evolution Reactions. *J. Mater. Chem. A* **2016**, *4* (47), 18272−18277.

(67) Hu, T.; Wang, Y.; Zhang, L.; et al. Facile Synthesis of PdO-doped Co_3O_4 Nanoparticles as an Efficient Bifunctional Oxygen Electrocatalyst. *Appl. Catal., B* **2019**, *243*, 175−182.

(68) Song, D.; Shin, J.; Lee, Y.; et al. Thin Nickel Layer with Embedded WC Nanoparticles for Efficient Oxygen Evolution. *ACS Appl. Energy Mater.* **2019**, *2* (5), 3452−3460.